Chemical Engineering Journal 450 (2022) 138450

Contents lists available at ScienceDirect

Chemical Engineering Journal

journal homepage: www.elsevier.com/locate/cej

Production of hydrogen from gas-phase ethanol dehydrogenation over iron-grafted mesoporous Pt/TiO_2 photocatalysts

Patricia García-Muñoz [a,*], Niels P. Zussblatt [b], Bradley F. Chmelka [b], Víctor A. de la Peña O'Shea [c], Fernando Fresno [c,d,*]

[a] Department of Industrial Chemical and Environmental Engineering, Escuela Técnica Superior de Ingenieros Industriales (ETSII), Universidad Politécnica de Madrid, 28006 Madrid, Spain
[b] Department of Chemical Engineering, University of California, Santa Barbara, CA 93106, United States
[c] Photoactivated Processes Unit, IMDEA Energy, 28935 Móstoles, Madrid, Spain
[d] Instituto de Catálisis y Petroleoquímica, CSIC, 28049 Madrid, Spain

ARTICLE INFO

Keywords:
Photocatalysis
Hydrogen
Mesoporous titania
Iron oxide
Acetaldehyde
Ethanol

ABSTRACT

We report the photocatalytic activity of iron-grafted mesoporous Pt/TiO_2 catalysts, combining the properties of heterojunction photocatalysts with mesoporosity, for the gas-phase production of hydrogen from water-ethanol mixtures. GC–MS analysis reveals a preferential ethanol dehydrogenation reaction pathway, resulting in the formation of acetaldehyde with high selectivity versus carbon dioxide, for all of the catalysts investigated. Multi-technique characterization reveals that, in all the iron-grafted samples, Fe is located predominantly on the surfaces of the catalysts as Fe_2O_3 rather than doping the anatase structure, while the mesoporosity of the starting TiO_2 is preserved. Among the different materials, the activity for photocatalytic ethanol dehydrogenation is optimum in the catalyst with the lowest iron content. According to XPS and time-resolved fluorescence measurements, this can be accounted for by higher Fe surface dispersion and consequent efficient formation of a surface heterojunction between Fe_2O_3 and TiO_2 that favours charge separation.

1. Introduction

Among the main obstacles to the implementation of hydrogen as an energy vector today are the challenges presented by its production from renewable feedstock and energy sources [1]. Once these challenges are overcome, hydrogen is expected to play a key role in a future energy mix that de-emphasizes fossil fuels, not only as a clean fuel itself, but also as a reagent for the obtainment of liquid fuels, for example from CO_2 [2]. However, to date, hydrogen is produced mostly from fossil fuels, mainly by natural gas reforming [3], which, although in the medium term may be environmentally tolerated if combined with capture, storage and recovery of CO_2, in the long term it is not suitable as a sustainable alternative. In this sense, to obtain fully renewable hydrogen, water can be used as the only raw material. Electrolysis therefore appears as a viable alternative and is currently a mature technology, although only *ca.* 0.03 % of hydrogen is produced by this method on a global scale [3]. In any case, to integrate hydrogen as a cost-effective vector in an energy system independent of fossil fuels, the source of electricity must also be renewable. This also presents a major challenge due to the enormous amount of electrical power needed from renewable sources to adopt electrolysis as an economically viable and sustainable means of large-scale hydrogen production [4].

Therefore, it is plausible to consider the incorporation of direct methods for the conversion of renewable energy, solar par excellence, into hydrogen, and here the decomposition of water by means of photocatalysis emerges as an appealing alternative [5]. This process is based on the surface reactivity towards adsorbed water of electron-hole pairs generated in a semiconductor upon absorption of photons with sufficient energy. This, however, is complicated from the electronic point of view, mainly with respect to the oxidation reaction, which involves the transfer of four electrons per molecule of oxygen generated and makes the process inefficient [6]. To alleviate this, a sacrificial agent, that is, an easily oxidizable species that acts as an electron donor, is generally added to water. Amines, alcohols and sulphite/sulphide mixtures are the most common types of reagents used for this purpose in research works [7]. However, even if such additives considerably increase the rate of hydrogen production, this also results in the consumption of reagents and the generation of by-products from the oxidation of the sacrificial

* Corresponding authors.
E-mail addresses: patricia.gmunoz@upm.es (P. García-Muñoz), fernando.fresno@csic.es (F. Fresno).

https://doi.org/10.1016/j.cej.2022.138450
Received 8 April 2022; Received in revised form 29 July 2022; Accepted 31 July 2022
Available online 3 August 2022

agent. Therefore, this strategy only makes practical sense, from an environmental and energy efficiency point of view, if aqueous waste or raw materials of renewable origin are used. Consequently, it is of high interest to use biomass derivatives for this purpose, which would allow closing a virtually CO_2 neutral cycle of storage and use of solar energy, framed into the recently proposed concept of a *photobiorefinery*, which implies not only the use of biomass-derived sacrificial reagents but also the simultaneous production of hydrogen and organic value-added products [8]. In this respect, ethanol is an interesting feedstock, as it can be obtained from waste lignocellulosic biomass. In addition to its direct use as biofuel, ethanol can alternatively be converted into hydrogen and a value-added product, such as acetaldehyde, by means of photo-dehydrogenation reactions. These considerations improve the economics of photocatalytic hydrogen production with respect to, for example, photo-reforming that conduces to the formation of CO_2 [9].

Regarding photocatalysts, anatase TiO_2 remains the most studied and applicable one due to a combination of characteristics including its relative activity compared to other semiconductors, (photo)chemical stability and low cost [10]. Nevertheless, there is much room for improvement, and overall strategies have focused either on overcoming its main drawback, *i.e.* being active only under UV light, by extending its activity to the visible spectrum, or on trying to improve as much as possible its efficiency in using the UV component of the solar spectrum. Among these strategies, doping with metals [11] and non-metals [12], co-catalyst deposition [13], micro- and mesostructuring [14], as well as the formation of composites or heterojunctions [15], have been explored. Regarding the latter, combining different semiconductors with TiO_2 is a very promising strategy for the improvement of photocatalytic reactions, because it offers a wide range of possibilities with regard to different compositions, crystal sizes or loading amounts of the second semiconductor, and can result in different positive effects such as improved charge separation, modified surface properties or enhanced adsorption capacity [16]. In particular iron is an interesting metal to combine with TiO_2 in photocatalytic applications, as it is highly abundant and does not present significant toxicity. Fe_2O_3, indeed, is an *n*-type semiconductor, although its low bandgap value and the positions of its valence and conduction bands limit its photocatalytic activity [17]. Nevertheless, the relative positions of its bands with respect to those of TiO_2 make it a promising candidate to promote the separation of photogenerated charge carriers and reduce their recombination [18].

Here, we report the photocatalytic activity of iron-grafted mesoporous TiO_2 catalysts for the production of hydrogen from gas-phase water–ethanol mixtures. These materials combine the properties mentioned above for heterojunction photocatalysts with mesoporosity [19], which is of particular interest in gas-phase reactions, like those described here, requiring high surface areas and adsorption capacities [20,21].

2. Materials and methods

2.1. Catalyst synthesis

Mesoporous titania ($mTiO_2$) samples were obtained by calcining a mesostructured composite of titania and a structure-directing surfactant [22]. The titania-surfactant composite was prepared by drying a mixture of titanium tetrachloride, ethanol, and a triblock-copolymer surfactant (Pluronic^{TM} F127, Sigma-Aldrich). As a general procedure, 1 g of the Pluronic^{TM} F127 was dissolved in 10 g of anhydrous ethanol. After complete dissolution, 1.90 g of $TiCl_4$ (Acros, 99.9 %) was added dropwise with vigorous stirring. The mixture was then poured into a Petri dish and dried for 7 days at 40 °C. Once drying was complete, the so-obtained titania-surfactant composite films were calcined in a ceramic crucible in an air atmosphere at 400 °C for 5 h, with heating and cooling ramp rates of 1 °C min^{-1}. This results in the removal of the structure-directing agent and the formation of a mesoporous titania powder.

Iron-grafted mesoporous titania catalysts (X Fe-$mTiO_2$, where X is the Fe wt.% from XPS) were obtained by adding 1 g of mesoporous titania powder to solutions with different quantities (80, 160, or 320 mg) of anhydrous $FeCl_3$ in 50 mL of anhydrous ethanol. The mixtures were stirred for 6 h, after which vacuum filtering gave yellowish powders that were subsequently dried at 90 °C for 6 h.

2.2. Characterization techniques

Nitrogen adsorption–desorption isotherms were recorded at 77 K in a MicroMeritics Tristar 3000 equipment, after degassing the samples overnight at 120 °C under flowing N_2. The surface areas were calculated by using the Brunauer-Emmett-Teller (BET) method, while pore volumes and pore size distributions were calculated by using the Barrett-Joyner-Halenda (BJH) method. X-ray diffraction (XRD) patterns were recorded in a Panalytical EMPYREAN diffractometer using CuK_α radiation (λ = 1.54178 Å) with a scanning rate of 0.01° s^{-1} and a step size of 0.013°. The iron and titanium bulk contents were determined by total reflection X-ray fluorescence (TXRF), using a FEI 8030c TXRF spectrometer. X-ray photoelectron spectra (XPS) were acquired on a Kratos Axis Ultra system. Surface elemental compositions were determined by averaging three survey scans over a range of 0 to 800 eV with a step size of 0.25 eV and a pass energy of 160 eV. Spectra were processed using Casa XPS software, and referenced to the position of the adventitious carbon C 1 *s* peak, set at 284.6 eV. Scanning electron microscopy (SEM) was conducted on a Hitachi TM 1000 table-top instrument operating at a constant voltage of 15 kV and equipped with an energy dispersive X-ray (XEDS) analyser. Field emission scanning electron microscopy (FE-SEM) characterization was performed by means of a JEOL JSM-7900F microscope using selective secondary electrons detection. The accelerating voltage was set at 1.0 kV to obtain high-resolution images and at 15 kV for elemental analysis with an Oxford Ultimate XEDS detector. Ultraviolet–visible diffuse reflectance spectra (UV–Vis DRS) of powdered samples were recorded on a Perkin Elmer Lambda 1050 UV/VIS/NIR equipment with a Praying Mantis diffuse reflectance accessory. Time-resolved fluorescence measurements were carried out by time-correlated single photon counting (TCSPC) with a Mini-τ equipment from Edinburgh Instruments. A laser of 372.2 nm wavelength and 61.2 ps pulse width was used for excitation, and a band-pass filter at 400 ± 25 nm was placed before the detector. Fluorescence lifetimes were calculated by fitting intensity decays to exponential decay curves.

2.3. Photocatalytic reactions

Prior to conducting hydrogen evolution experiments, platinum was photo-deposited on all samples as a co-catalyst. For that purpose, the powdered oxides were suspended in a 10 vol% aqueous methanol solution containing the appropriate dissolved amount of H_2PtCl_6 for 0.5 wt % Pt in the final material and, after purging with an argon flow (60 cm^3 min^{-1}), irradiated with a medium pressure mercury immersion lamp (λ_{max} 365 nm) until hydrogen was detected by an in-line Agilent 490 micro-GC with a MS5A PLOT column and a TCD detector (20 min irradiation in average). The solid products were then separated by filtration and dried at 90 °C overnight.

Gas-phase ethanol photocatalytic dehydrogenation reactions were carried out in a stainless steel reactor (10.8 cm^3) with a borosilicate glass window for irradiation, which was provided by two 2.9 W LEDs with emission centred at 365 nm. The powdered Pt-loaded catalysts (5 mg) were deposited on glass microfibre filters from ethanolic suspensions and fitted into the reaction chamber. The reactor was fed by an argon flow (20 cm^3 min^{-1}) that was previously bubbled through a 10 vol% aqueous ethanol solution kept at 60 °C, giving rise to gas concentrations of 1.5 and 16 vol% for ethanol and water, respectively, according to Raoult's law and Antoine's equation [23]. The reactor was kept at the same temperature to avoid condensation. Hydrogen concentrations at the outlet of the reactor were determined by in-line mass spectrometry (MS) by monitoring the ion with an *m/z* ratio of 2. The rest of reaction

Table 1
Physico-chemical characteristics of the studied catalysts.

Catalyst	Crystal phases	S_{BET} (m^2g^{-1})	Pore width (A)	Ti wt.%		Fe wt.%		
				Surface[a]	Bulk[b]	Surface[a]	Bulk[b]	Surf/bulk
$mTiO_2$	Anatase	178	140	59.9	57.8	0.0	0.0	–
1.0Fe-$mTiO_2$	Anatase	172	132	59.6	57.5	1.0	0.05	20
1.5Fe-$mTiO_2$	Anatase	165	130	58.8	57.8	1.5	0.08	18.75
2.1Fe-$mTiO_2$	Anatase	158	140	58.1	57.8	2.1	0.12	17.5

[a] From XPS; [b] From TXRF.

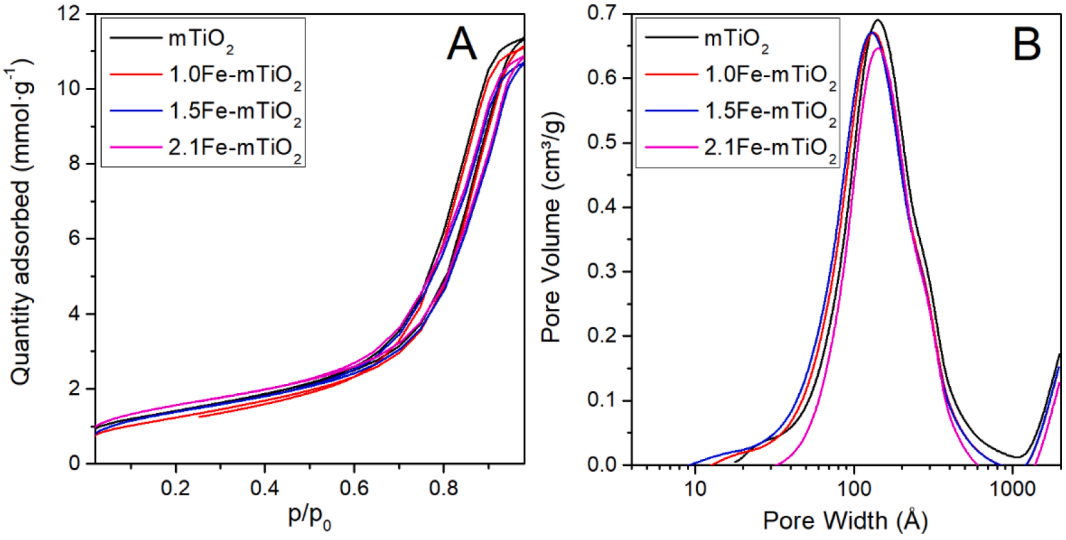

Fig. 1. (A) N_2 sorption isotherms at 77 K and (B) BJH pore size distributions.

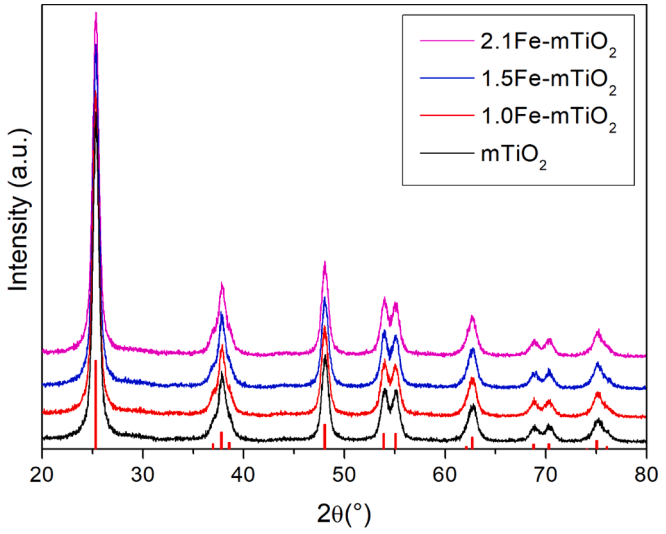

Fig. 2. Wide-angle XRD patterns of the mesoporous titania and iron-grafted materials. Red bars indicate the Bragg reflections corresponding to the anatase TiO_2 phase (ICDD PDF # 21–1272).

products were analyzed by means of an Agilent 7820A gas chromatograph equipped with a GS-Carbon-PLOT column and connected to a 5977B mass spectrometry detector with electron impact ionization. A scheme of the full system is shown in Supplementary Material, Figure S1. The oxidation reaction selectivities towards acetaldehyde were calculated as $S_{AcH} = r_{AcH} / (r_{AcH} + 2\, r_{CO2})$, being *S* selectivity and *r* formation molar rates.

3. Results and discussion

3.1. Catalyst characterization

The main physicochemical characteristics of the synthesized mesoporous catalysts are collected in Table 1. The synthesized titania ($mTiO_2$) shows a type-IV nitrogen sorption isotherm (Fig. 1A), confirming its mesoporous nature, with a pore size distribution centred at 14 nm (Fig. 1B) and a BET surface area of approximately 180 m^2g^{-1}. Inclusion of iron does not modify the shape of the isotherms, but slightly decreases the mean pore size and the surface area, suggesting that iron species partly cover the catalyst surface. Indeed, the surface iron contents determined from XPS measurements, upon which the samples have been distinguished and labelled, are considerably larger than the bulk values found from X-ray fluorescence, indicating that iron is concentrated at the surface of the catalysts. This could be expected, by taking into account the soft method employed for the preparation of the iron-grafted catalysts. In addition, the surface/bulk iron ratios displayed in Table 1 reveal a higher relative surface exposure of iron species in samples with lower loading. For all of the iron-grafted mesoporous TiO_2 samples examined, the high-resolution Fe 2*p* XPS spectra (Fig. S2) exhibit photoemission features that closely resemble those of Fe(III) in Fe_2O_3 [24].

The wide-angle X-ray diffraction patterns of mesoporous TiO_2 in Fig. 2. show reflections at 24.8°, 37.3°, 48.1°, 54.2°, and 62°, which are indexable to the anatase phase compared to ICDD PDF no. 21–1272. The iron-containing materials show diffraction patterns with no significant differences to those of iron-free TiO_2. Thus, no additional reflections attributable to iron phases are observed in any of the samples, in accordance with the low bulk iron concentrations obtained from TXRF (Table 1). Fitting the diffraction profiles to the reference pattern mentioned above results in cell parameters without a monotonic

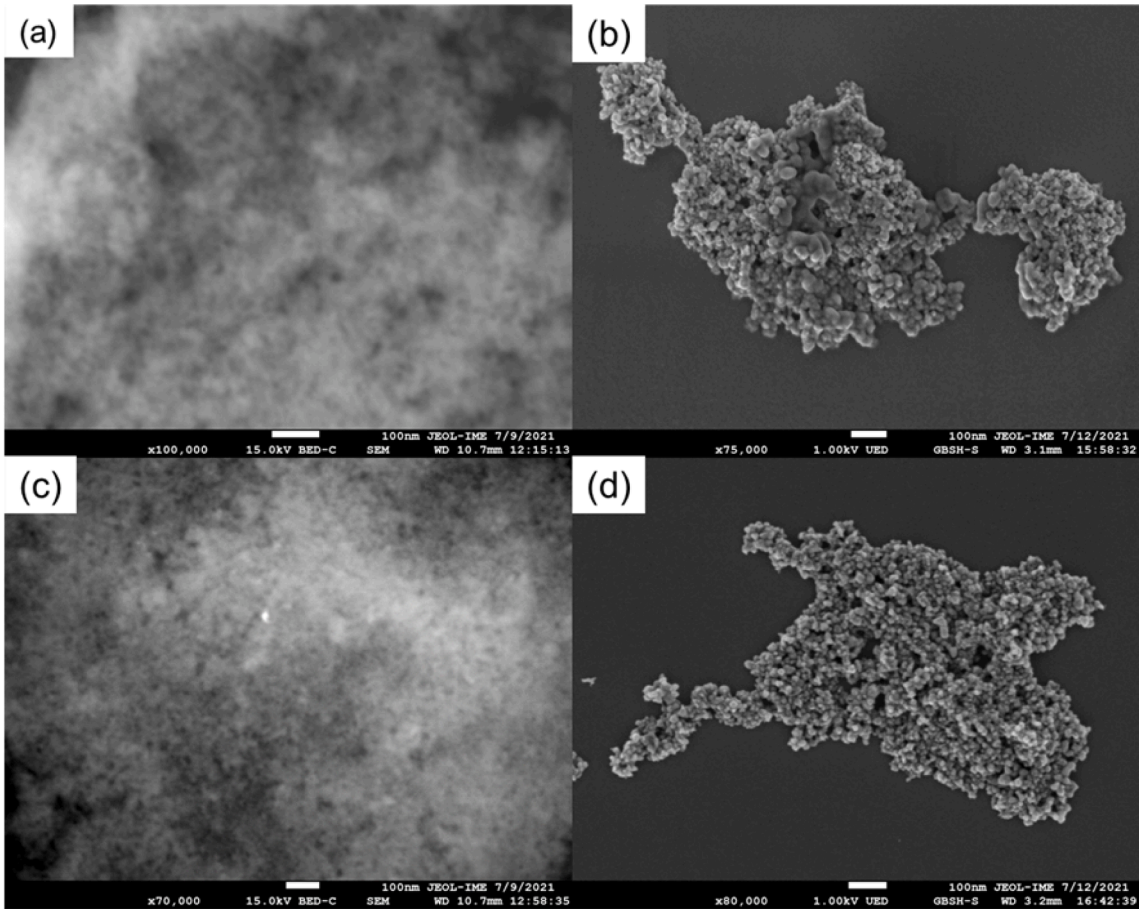

Fig. 3. FE-SEM images of $mTiO_2$ (a, b) and 1.0Fe-$mTiO_2$ (c, d).

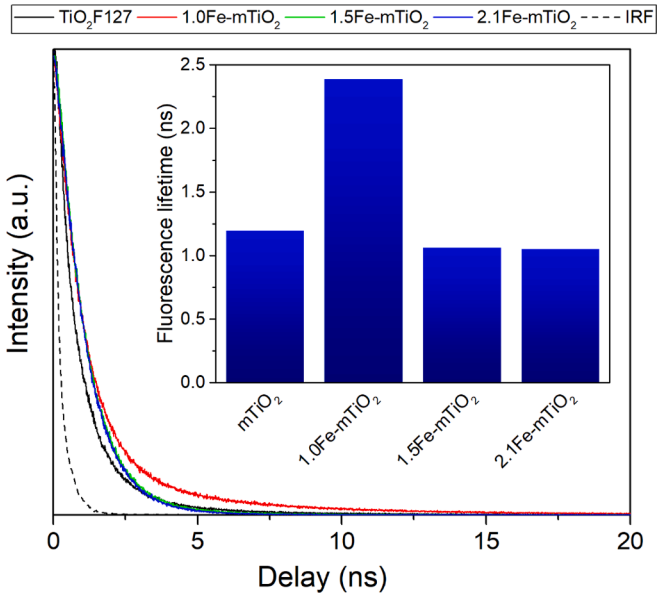

Fig. 4. Fluorescence temporal decay curves of the studied catalysts. The dashed line represents the instrument response function. Inset: fluorescence lifetimes calculated from exponental decay fittings.

increase upon iron loading within the uncertainty of the measurements (Fig. S3). This suggests that Fe is grafted principally on the surface of TiO_2, without iron doping into the TiO_2 structure, as could be expected from the method of synthesis and in agreement with the observations from XPS. In addition, all samples present a similar nanocrystallite size of anatase as determined from XRD with the Scherrer equation (12.2–12.5 nm), reinforcing the idea that no inclusion of iron into the anatase structure occurs. SEM images (Fig. S4) show agglomerates of different sizes in all samples, regardless of the presence or amount of iron. The texture of the larger particles in the higher magnification images suggests that they are clumps of smaller particles. EDX analyses show the presence of iron in all the analyzed areas of the iron-loaded catalysts. Larger magnification FE-SEM images of $mTiO_2$ (Fig. 3) show particles formed by crystal agglomeration with an inter-crystal mesopore structure with a pore size range in good agreement with the nitrogen sorption isotherms. This texture is maintained after iron loading, also in agreement with Fig. 1.

With regard to optoelectronic properties, diffuse reflectance UV–vis spectra (Fig. S5) show the onset of photoabsorption by mesoporous TiO_2 at approx. 405 nm, as expected for the anatase phase [25]. In contrast, Fe_2O_3-TiO_2 mesoporous materials show additional photoabsorption as a shoulder in the short-wavelength (high-energy) region (400–600 nm) of the visible spectrum, with intensity increasing with higher iron load, consistently with the presence of Fe_2O_3 [26] and with the change in the colour of the catalysts from white for pure TiO_2 to light yellow for the iron-containing samples. Deconvolution of this shoulder reveals essentially identical spectra for TiO_2 in all samples, manifesting an unmodified titania band gap, in accordance with the absence of iron doping. Time-resolved fluorescence measurements (Fig. 4) were used to calculate the lifetime of the fluorescence due to TiO_2 upon UV excitation. As shown in the inset of Fig. 4, inclusion of iron over mesoporous TiO_2 in the lowest amount results in a considerable increase in fluorescence lifetime compared to $mTiO_2$. This can be accounted for by slower

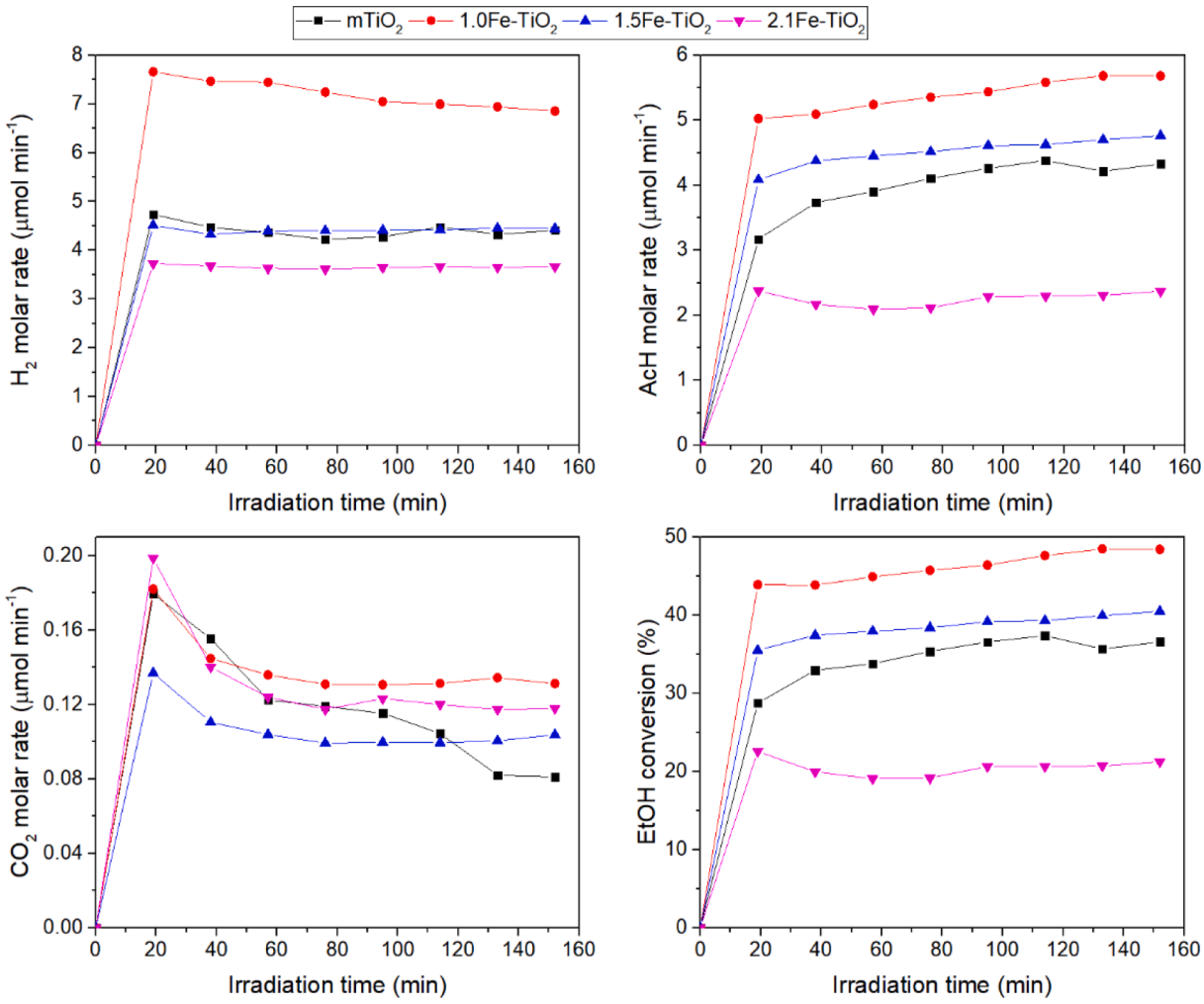

Fig. 5. Formation rates of the different gas-phase reaction products and ethanol conversions over the studied catalysts. Reaction conditions: continuous flow, 5 mg catalyst, $[EtOH]_0$ = 1.5 vol%, $[H_2O]_0$ = 16 vol%, λ_c = 365 nm.

electron-hole recombination [27], which, in the presence of two semiconducting phases, can be interpreted in terms of inter-phase charge transfer: increased lifetime would imply either a higher number of photoexcited electrons in the conduction band of TiO_2 or a lower number of photogenerated holes in the valence band [28]. Given the relative band energies between TiO_2 and Fe_2O_3 (see Fig. S6), it seems plausible to deduce a direct *Z*-scheme in which photoexcited electrons in Fe_2O_3 recombine with photogenerated holes in TiO_2 [15], as depicted in Fig. S6(a). However, with very small crystal sizes in which quantum size effects take place, a type-I heterojunction situation, like the one described in Fig. S6(b), might be expected [18]. On the other hand, higher amount of iron apparently contributes to the loss of the charge separation effect observed for the lowest Fe loading, suggesting that an adequate contact between phases to produce such charge transfer occurs only with low iron quantity. Comparing with XPS data, it seems reasonable to assume that the higher iron surface dispersion for lower iron loadings favours this phase contact.

3.2. Photocatalytic hydrogen evolution

Gas-phase photocatalytic reactions in an argon flow saturated with ethanol and water gave rise to hydrogen, acetaldehyde and CO_2 as the only products detected in the gas phase at the reactor outlet. The same products were detected for all of the studied catalysts, indicating that iron grafting of titania does not change the reaction qualitatively. As measured by real-time mass spectrometry, hydrogen evolution starts immediately after irradiation begins and ceases when the UV source is turned off, as shown in Fig. S7 for the 1Fe-$mTiO_2$ catalyst, indicating the photocatalytic nature of the reaction.

Table 2
Reaction selectivities and stoichiometries after 160 min.

Catalyst	Selectivity to AcH (%)	H_2/AcH molar ratio	Produced H_2/Consumed EtOH
$mTiO_2$	96.3	1.02	0.98
1.0Fe-$mTiO_2$	95.5	1.21	1.15
1.5Fe-$mTiO_2$	96.2	0.93	0.94
2.1Fe-$mTiO_2$	90.6	1.54	1.41

Fig. 5 shows the evolution rates of the three detected gas-phase reaction products as functions of irradiation time for the different tested catalysts. Regarding product distribution, it can be clearly seen that, in all cases, the main ethanol oxidation product is acetaldehyde, which is produced in one order of magnitude larger amount than carbon dioxide, as is also reflected by the reaction selectivities towards AcH against CO_2, close to 100 % over all the studied catalysts (Table 2). This also indicates that, for all of the catalysts investigated, the preferred path for photocatalytic hydrogen evolution in the present conditions is ethanol dehydrogenation (Reaction (1)) against ethanol photo-reforming (Reaction

(2)) or even acetaldehyde photoreforming (Reaction (3)). The obtained hydrogen/acetaldehyde molar ratios are also all close to the ethanol dehydrogenation stoichiometry, and so are the ratios of hydrogen to converted ethanol (both in Table 2), which are much closer to the value of 1 for Reaction (1) than to 6 for Reaction (2). In this sense, hydrogen production exceeding the stoichiometry of Reaction (1) may be related to the contribution of Reaction (2) or to the production of undetected or surface adsorbed products (e.g. acetates), while lower hydrogen production can be associated to the occurrence of a water gas shift reaction (Reaction (4)), which would nevertheless further increase the apparent selectivity to AcH vs CO_2 by consuming carbon dioxide. The latter reaction would also be accompanied by the production of CO, which can remain undetected with the present analytical conditions.

$$CH_3CH_2OH \rightleftarrows CH_3CHO + H_2 \quad (1)$$

$$CH_3CH_2OH + 3\ H_2O \rightleftarrows 2\ CO_2 + 6\ H_2 \quad (2)$$

$$CH_3CHO + 3\ H_2O \rightleftarrows 2\ CO_2 + 5\ H_2O \quad (3)$$

$$CO_2 + H_2 \rightleftarrows CO + H_2O \quad (4)$$

In any case, the resulting product distributions, as stated above, manifest a selective reaction of ethanol dehydrogenation, as has been previously reported for similar reaction conditions [29,30]. In other reports, reactions with pure ethanol or lower water/ethanol ratios have led preferentially to the photo-reforming pathway, with H_2 and CO_2 as main products, and ethylene arising from ethanol dehydration [31].

Quantitatively, the constant hydrogen production rates obtained for all of the catalysts indicate that catalyst deactivation does not occur to a significant extent over the range of reaction time studied. Mesoporous TiO_2 itself outperforms the well-known commercial TiO_2 P25 tested in the same reactor and under the same reaction conditions [32], and its hydrogen evolution rate is similar to those obtained with TiO_2 catalysts supported on mesoporous silica SBA-15 [20], revealing the positive effect of the mesoporosity, which is attained in the present samples without the need for a support. The inclusion of iron results, for the sample with 1 wt% in the surface, in increased photocatalytic activity as reflected by the higher hydrogen production rate and both acetaldehyde production and ethanol conversion. This improvement is lost, however, with higher iron loading, so that the activity of the 1.5Fe-mTiO_2 catalyst is very similar to that of mTiO_2 with respect to the different parameters shown in Fig. 5. Further increasing the quantity of surface iron to 2 % results in a detrimental effect on photoactivity, as observed from the comparison of the curves corresponding to the 2.1Fe-mTiO_2 sample.

As is common when combining two different semiconductors in photocatalysis [16], the concurrence of different opposed effects may explain the photocatalytic behaviour of the present heterojunctions. As is evident from the comparison of Figs. 4 and 5, the interfacial charge separation deduced from fluorescence lifetimes is in good accordance with the improved photocatalytic activity attained with the lowest iron loading and can be invoked as the main reason for the activity of the optimized activity of 1Fe-mTiO_2 catalyst. Once the improved charge separation is lost with increasing iron loading, detrimental effects, such as decreased surface area (Table 1), or simply the presence beyond the optimum amount of an oxide that is *per se* less active than TiO_2 [33], may come into play resulting finally in a reduced activity of 2.1Fe-mTiO_2 catalyst.

4. Conclusions

Iron-modified mesoporous TiO_2 photocatalysts have been obtained by a soft method. As deduced from nitrogen sorption isotherms, X-ray diffraction, X-ray photoelectron spectroscopy, UV–vis diffuse reflectance spectra and scanning electron microscopy, iron is located predominantly on the surfaces of the catalysts as Fe_2O_3 rather than doping the anatase structure, while the mesoporosity of the starting TiO_2 is preserved. Time-resolved fluorescence measurements reveal increased fluorescence lifetime with an optimum surface iron loading of 1 wt%, in which iron surface dispersion is higher, from which the formation of a surface heterojunction between Fe_2O_3 and TiO_2 and consequent charge separation can be deduced. Higher iron amounts, however, are associated with the loss of improved charge separation. As a result, the activity of iron-grafted mesoporous titania catalysts for photocatalytic hydrogen production from water-ethanol solutions is optimum in the catalyst in which such heterojunction occurs. Regarding ethanol oxidation products, GC–MS analysis reveals the prevalence of the ethanol dehydrogenation reaction pathway, resulting in the formation of acetaldehyde with high selectivity versus carbon dioxide, for all of the catalysts tested.

Declaration of Competing Interest

The authors declare that they have no known competing financial interests or personal relationships that could have appeared to influence the work reported in this paper.

Data availability

Data will be made available on request.

Acknowledgements

This work has received financial support from Spanish MCIN/AEI/10.13039/501100011033 and "ERDF A way of making Europe", through projects PID2020-118593RB-C22 and ENE2017-89170-R, from Comunidad de Madrid and European Structural Funds through FotoArt-CM project (S2018/NMT-4367) and from the European Research Council (ERC) through the HyMAP project, grant agreement no. 648319. The work at UCSB was supported by the Institute for Collaborative Biotechnologies through Grant No. W911NF-09-0001 from the U. S. ARO. The content of the information does not necessarily reflect the position or the policy of the U.S. Government, and no official endorsement should be inferred. Technical assistance by Dr. F. Picó for FE-SEM and XRD measurements, and by Mr. M. J. Ortega and Mr. A. Benito for photocatalytic reactions, is gratefully acknowledged.

Appendix A. Supplementary data

Supplementary data to this article can be found online at https://doi.org/10.1016/j.cej.2022.138450.

References

[1] N. Armaroli, V. Balzani, The hydrogen issue, ChemSusChem 4 (2011) 21–36, https://doi.org/10.1002/cssc.201000182.
[2] D.G. Nocera, Solar fuels and solar chemicals industry, Acc. Chem. Res. 50 (2017) 616–619, https://doi.org/10.1021/acs.accounts.6b00615.
[3] IEA, Hydrogen, Paris, 2021. https://www.iea.org/reports/hydrogen.
[4] G.H. Rau, H.D. Willauer, Z.J. Ren, The global potential for converting renewable electricity to negative-CO2-emissions hydrogen, Nat. Clim. Change. 8 (2018) 621–625, https://doi.org/10.1038/s41558-018-0203-0.
[5] J. Dufour, D.P. Serrano, J.L. Gálvez, A. González, E. Soria, J.L.G. Fierro, Life cycle assessment of alternatives for hydrogen production from renewable and fossil sources, Int. J. Hydrog. Energy. 37 (2012) 1173–1183, https://doi.org/10.1016/j.ijhydene.2011.09.135.
[6] F. Fresno, R. Portela, S. Suárez, J.M. Coronado, Photocatalytic materials: recent achievements and near future trends, J Mater Chem A. 2 (2014) 2863–2884, https://doi.org/10.1039/C3TA13793G.
[7] F. Costantino, P.V. Kamat, Do sacrificial donors donate H2 in photocatalysis? ACS Energy Lett. 7 (2022) 242–246, https://doi.org/10.1021/acsenergylett.1c02487.
[8] T. Butburee, P. Chakthranont, C. Phawa, K. Faungnawakij, Beyond artificial photosynthesis: prospects on photobiorefinery, ChemCatChem 12 (7) (2020) 1873–1890.
[9] C. Ampelli, C. Genovese, R. Passalacqua, S. Perathoner, G. Centi, A gas-phase reactor powered by solar energy and ethanol for H2 production, Appl. Therm. Eng. 70 (2014) 1270–1275, https://doi.org/10.1016/j.applthermaleng.2014.04.013.
[10] L. Biswal, R. Mohanty, S. Nayak, K. Parida, Review on MXene/TiO2 nanohybrids for photocatalytic hydrogen production and pollutant degradations, J. Environ. Chem. Eng. 10 (2) (2022) 107211.

[11] N.S. Ibrahim, W.L. Leaw, D. Mohamad, S.H. Alias, H. Nur, A critical review of metal-doped TiO2 and its structure–physical properties–photocatalytic activity relationship in hydrogen production, Int. J. Hydrog. Energy. 45 (2020) 28553–28565, https://doi.org/10.1016/j.ijhydene.2020.07.233.
[12] M. Pelaez, N.T. Nolan, S.C. Pillai, M.K. Seery, P. Falaras, A.G. Kontos, P.S. M. Dunlop, J.W.J. Hamilton, J.A. Byrne, K. O'Shea, M.H. Entezari, D.D. Dionysiou, A review on the visible light active titanium dioxide photocatalysts for environmental applications, Appl. Catal. B Environ. 125 (2012) 331–349, https://doi.org/10.1016/j.apcatb.2012.05.036.
[13] S. Bai, W. Yin, L. Wang, Z. Li, Y. Xiong, Surface and interface design in cocatalysts for photocatalytic water splitting and CO 2 reduction, RSC Adv. 6 (2016) 57446–57463, https://doi.org/10.1039/C6RA10539D.
[14] W. Li, Z. Wu, J. Wang, A.A. Elzatahry, D. Zhao, A Perspective on Mesoporous TiO2 Materials, Chem. Mater. 26 (2014) 287–298, https://doi.org/10.1021/cm4014859.
[15] K. Perović, F.M. dela Rosa, M. Kovačić, H. Kušić, U.L. Štangar, F. Fresno, D. D. Dionysiou, A. Loncaric Bozic, Recent achievements in development of TiO2-based composite photocatalytic materials for solar driven water purification and water splitting, Materials. 13 (6) (2020) 1338.
[16] F. Fresno, Heterojunctions: Joining different semiconductors, Green Energy Technol. 71 (2013) 311–327, https://doi.org/10.1007/978-1-4471-5061-9_15.
[17] M. Mishra, D.-M. Chun, α-Fe2O3 as a photocatalytic material: A review, Appl. Catal. Gen. 498 (2015) 126–141, https://doi.org/10.1016/j.apcata.2015.03.023.
[18] A. Kubacka, M. Fernández-García, G. Colón, Advanced nanoarchitectures for solar photocatalytic applications, Chem. Rev. 112 (2012) 1555–1614, https://doi.org/10.1021/cr100454n.
[19] P. García-Muñoz, N.P. Zussblatt, G. Pliego, J.A. Zazo, F. Fresno, B.F. Chmelka, J. A. Casas, Evaluation of photoassisted treatments for norfloxacin removal in water using mesoporous Fe2O3-TiO2 materials, J. Environ. Manage. 238 (2019) 243–250.
[20] N.L. Torres-Garcia, F. Fresno, F.E. Oropeza, R. Huirache-Acuña, V.A. Peña-O'Shea, Effect of the TiO2 Nanocrystal Dispersion Over SBA-15 in the Photocatalytic H2 Production Using Ethanol as Electron Donor, Adv. Sustain. Syst. 5 (2021) 2100133, https://doi.org/10.1002/adsu.202100133.
[21] L. Collado, I. Jansson, A.E. Platero-Prats, V. Perez-Dieste, C. Escudero, E. Molins, L. Casas i Doucastela, B. Sánchez, J.M. Coronado, D.P. Serrano, S. Suarez, V.A. de la Peña-O'Shea, De La Peña-O'Shea, Elucidating the Photoredox Nature of Isolated Iron Active Sites on MCM-41, ACS Catal. 7 (3) (2017) 1646–1654.
[22] P. Yang, D. Zhao, D.I. Margolese, B.F. Chmelka, G.D. Stucky, Block Copolymer Templating Syntheses of Mesoporous Metal Oxides with Large Ordering Lengths and Semicrystalline Framework, Chem. Mater. 11 (1999) 2813–2826, https://doi.org/10.1021/cm990185c.
[23] C. Sapsanis, H. Omran, V. Chernikova, O. Shekhah, Y. Belmabkhout, U. Buttner, M. Eddaoudi, K. Salama, Insights on Capacitive Interdigitated Electrodes Coated with MOF Thin Films: Humidity and VOCs Sensing as a Case Study, Sensors. 15 (2015) 18153–18166, https://doi.org/10.3390/s150818153.
[24] J. Fragoso, D. Barreca, L. Bigiani, A. Gasparotto, C. Sada, O.I. Lebedev, E. Modin, I. Pavlovic, L. Sánchez, C. Maccato, Enhanced photocatalytic removal of NOx gases by β-Fe2O3/CuO and β-Fe2O3/WO3 nanoheterostructures, Chem. Eng. J. 430 (2022), 132757, https://doi.org/10.1016/j.cej.2021.132757.
[25] G. Longo, F. Fresno, S. Gross, U.L. Štangar, Synthesis of BiVO4/TiO2 composites and evaluation of their photocatalytic activity under indoor illumination, Environ. Sci. Pollut. Res. 21 (2014) 11189–11197, https://doi.org/10.1007/s11356-014-2624-2.
[26] B. Palanisamy, C.M. Babu, B. Sundaravel, S. Anandan, V. Murugesan, Sol–gel synthesis of mesoporous mixed Fe2O3/TiO2 photocatalyst: Application for degradation of 4-chlorophenol, J. Hazard. Mater. 252–253 (2013) 233–242, https://doi.org/10.1016/j.jhazmat.2013.02.060.
[27] J. Liqiang, Q. Yichun, W. Baiqi, L. Shudan, J. Baojiang, Y. Libin, F. Wei, F. Honggang, S. Jiazhong, Review of photoluminescence performance of nano-sized semiconductor materials and its relationships with photocatalytic activity, Sol. Energy Mater. Sol. Cells. 90 (2006) 1773–1787, https://doi.org/10.1016/j.solmat.2005.11.007.
[28] U. Noomnarm, R.M. Clegg, Fluorescence lifetimes: Fundamentals and interpretations, Photosynth. Res. 101 (2009) 181–194, https://doi.org/10.1007/s11120-009-9457-8.
[29] C. Ampelli, R. Passalacqua, C. Genovese, S. Perathoner, G. Centi, T. Montini, V. Gombac, J.J. Delgado Jaen, P. Fornasiero, H2 production by selective photo-dehydrogenation of ethanol in gas and liquid phase on CuOx/TiO2 nanocomposites, RSC Adv. 3 (2013) 21776–21788, https://doi.org/10.1039/c3ra22804e.
[30] C. Dessal, L. Martínez, C. Maheu, T. Len, F. Morfin, J.L. Rousset, E. Puzenat, P. Afanasiev, M. Aouine, L. Soler, J. Llorca, L. Piccolo, Influence of Pt particle size and reaction phase on the photocatalytic performances of ultradispersed Pt/TiO2 catalysts for hydrogen evolution, J. Catal. 375 (2019) 155–163, https://doi.org/10.1016/j.jcat.2019.05.033.
[31] S. Murcia-López, M. González-Castaño, C. Flox, J.R. Morante, T. Andreu, On the role of Cu, Ag and Pt in active titania for gas-phase ethanol photo-reforming, Mater. Sci. Semicond. Process. 73 (2018) 30–34, https://doi.org/10.1016/j.mssp.2017.06.009.
[32] M.A. Esteves, F. Fresno, V.R. Fernandes, F.E. Oropeza, V.A. de la Peña O'Shea, C. M. Rangel, TiO2-reduced graphene oxide-Pt nanocomposites for the photogeneration of hydrogen from ethanol liquid and gas phases, Catal. Today. 380 (2021) 41–52, https://doi.org/10.1016/j.cattod.2021.05.012.
[33] M.D. Hernández-Alonso F. Fresno S. Suárez J.M. Coronado Development of alternative photocatalysts to TiO2: Challenges and opportunities Energy Environ. Sci. 2 2009 1231 1231 10.1039/b907933e.